Dynamic Studies of Small Animals with a Four-Color DOT Imager

Christoph H. Schmitz[1,2], Harry L. Graber[2], Mark Stewart[3], Rita D. Levina[1], Mikhail B. Levin[2], Yaling Pei[1], Yong Xu[1,2], and Randall L. Barbour[1,2]

[1]NIRx Medical Technologies LLC / 15 Cherry Lane / Glen Head, NY 11545 / cschmitz@nirx.net; [2]Dept. of Pathology, [3]Dept. of Physiology and Pharmacology / SUNY Downstate Medical Center / 450 Clarkson Ave. Brooklyn, NY 11203

ABSTRACT

We introduce a four-wavelength dynamic optical tomography system for small animal studies. A stereotaxic small animal measuring head was developed, which allows imaging of any body site of the animal. We present a setup for non-invasive dynamic optical imaging of the rat brain. The measuring head as well as the fiberoptics are compatible with in-magnet studies.

We give a detailed description of the implementation of the four-wavelength capability and the newly developed imaging head. A variety of system check procedures are presented that were developed to assess instrument functionality and data integrity for the device. Instrument performance parameters that are obtained with these tools – such as noise, short-, and long-term stability – are given. We also show results from a phantom-based calibration protocol to account for inter-channel variations of the system.

We present initial experimental results from dynamic optical measurements of the physiologic response of the rat brain to electric paws stimulation. The hemodynamic response in the brain for different stimulation sites is discussed. The results demonstrate excellent sensitivity of the instrument for measuring hemodynamics in small animal studies.

INSTRUMENTATION

The instrument developed is based on the NIRx DYNOT imaging platform, which has been described in detail before [1,2]. Key features of the device include:

- Continuous wave (cw) Diffuse Optical Tomographic (DOT) measurements @ 2- 75 frames per second depending on number of sources.
- Time division multiplexing of up to 32 sources (S)
- Parallel readout of up to 32 detectors (D)
- Parallel measurement of up to four frequency-encoded wavelengths (WL)
- Dynamic detection range 1:10[9] (90 dB_{opt}) through source-synchronized detector gain switching
- Current applications: Mammography, imaging of peripheral vasculature, functional brain imaging, small animal imaging.

1) HARDWARE

i. Four-Wavelength Capability

The following modifications were made to achieve simultaneous s four-color laser operation:

- Model 8000 laser diode controller (Newport Corp.) used in DYNOT accommodates modules for independent control of up to four thermo-electrically cooled laser diodes.
- Lasers used: 725 nm (250 mW_{max}), 760 nm, 810 nm, 860 nm (all 400 mW_{max})
- Lasers are mounted in compact "sandwich" configuration to save space and to allow efficient forced air cooling with fan.
- DYNOT standard power supply can be used without modification.

The optical switch (OS) is identical in design and function to the device in the previously described dual-wavelength imager [1]. Four-color operation of the OS was achieved by developing a new incoupling optics with the following features (see Fig. 1):

- Four-wavelength mixer/incoupler combines and focuses laser beams into optical switch.
- Custom made dichroic mirrors (Omega Optical, Inc.) allow efficient (90% typ.) wavelength multiplexing.
- Laser delivery fibers and the dichroic mirrors are individually adjustable (translation, tilt) to achieve optimum beam collinearity and centricity with respect to the OS.

The DYNOT programmable multi-channel optical detector (PMOD) is designed to allow simultaneous detection of up to four frequency-encoded optical signals. The following upgrades to the detection side of the system were performed for four-wavelength operation:

- A second lock-in module was added to each of the 32 detector channel boards to upgrade from dual- to quad-wavelength detection.
- A second phase shifter module was installed into the PMOD to condition the two additional reference signals for lock-in detection
- To acquire data from up to 128 measurement channels (= 4 WL × 32 detectors), a second 64-channel data acquisition (DAQ) board (National Instruments PCI6033E) was installed into the control PC.
- A new interface board was developed for the PMOD that accommodates connections to the two DAQ boards.

ii. MRI compatible Small Animal Imaging Head

The following hardware developments make the instrument compatible with in-magnet studies:

- 12 feet long fiber optic cables used for light transmission between instrument and target to keep instrument in safe distance from magnet.
- Illumination bundle diameter = 0.8 mm , detection bundle diameter 1.0 mm, probe end diameter = 2.0 mm
- No metal components used in fiber optics (plastic probe ferrules)
- No metal components used in animal holder

An imaging head was designed to ensure stable position of the animal and good optical probe contact (see Fig. 2).

- Stereotaxic positioning of the animal using ear bars and bite bar
- Fiber holder allows high-density arrangement of probes (3-mm center-to-center spacing)
- Foam cushion in fiber holder allows easy adjustment of probe pressure
- Special mouth piece bends 30° upward to make contact with roof of the mouth
- Fiber probes integrated into ear bars

2) SOFTWARE

The DYNOT control software is implemented in the LabVIEW language (National Instruments, Inc.) and has been described in detail before for the case of dual wavelength operation [2]. The software was upgraded to expand all existing features for the case of four-wavelength data sets:

- Setup Screen: Main function is the automated or manual adjustment of detector gain settings for all source-detector pairs to prepare the instrument for a measurement. Contains "Setup Check" feature to confirm probe contact fidelity, proper hardware function, and appropriateness of gain settings.
- Measurement Screen: Displays raw data in real time for all wavelengths.
- System Checkout Screen: Contains a variety of automated or semi-automated data and hardware integrity checks, including:
  - Detector dark noise measurement
  - Optical alignment tools for the optical switch
  - Instrument calibration procedures

DATA INTEGRITY AND PERFORMANCE CHECK PROCEDURES

- Because the imaging problem is ill-posed and under-determined, it is of paramount importance that data collection be performed with the highest precision and accuracy possible
  - ⇨ Requires all hardware components to be intact and to perform according to specified quality standards.
  - ⇨ Requires proper setup of optical measurement(e.g., appropriate gain settings, good probe-tissue contact).
- Large number of data channels (*i.e.*, up to 32S × 32D × 4 WL = 4096 channels) requires:
  - Automated or semi-automated test procedures to reduce test time and to increase reliability.
  - Easy-to-read visualization of complex results.

1) GAIN SETTINGS

Gain settings for each S-D pair need to be established before each measurement. Channels with improper gain setup may experience excessive noise or signal saturation/distortion. Several methods of testing the gain setup exist:

1. Gain settings for each S-D pair are displayed in a color-contour plot (see Fig. 3A). Deviations from application-characteristic pattern is indicative of inappropriate gain setting.
2. Because of the reciprocity of light transport, gains for reciprocal S - D channels, (i.e. S_m - D_n vs. S_n - D_m) are expected to be similar. For each S-D pair, the difference in gain for its reciprocal pair is calculated and displayed in a color-encoded contour plot. A difference greater than one gain step is indicative of inappropriate setup (Fig. 3B).

2) CORRELATION ANALYSIS

- For a time series of data, the correlation coefficient *r* between reciprocal S-D pairs is computed and graphed in a color contour plot.
- Non-random variation of physiologic data leads to high correlation values for reciprocal channels with high signal-to-noise ratio (Fig. 4A).
- Data are low-pass filtered to mitigate the influence of random detection noise (Fig. 4B)
- Isolated low *r* values are indicative of bad fiber-tissue contact

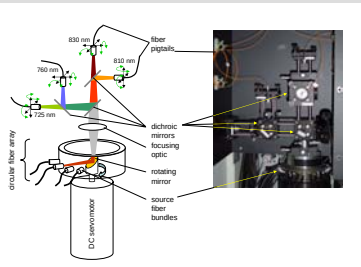

Fig. 1. Optical switch with four-wavelength mixer/incoupler.

Fig. 2. Stereotaxic rat imaging stage. A: Detailed view of the imaging head and the optical probes. B: Position of animal in the device and placement of optical fibers on the head.

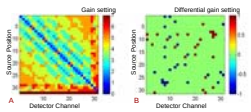

Fig. 3. System setup checks: A: Color encoded display of gain settings; notice the symmetric pattern. B: Color encoded display of differences between gain settings of reciprocal channels. Deviation by more than one step (not shown) is indicative of faulty setup.

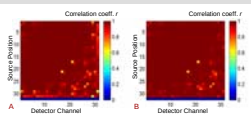

Fig. 4. Correlation values for physiologic time series of reciprocal channels. Strong positive correlation (values greater 0.8) are expected for reciprocal pairs not showing noise-dominated readings. A: Unfiltered result. B: Correlation result after low-pass filtering the data. Note the increased *r* values in the lower left compared to A.

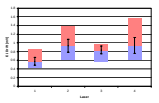

Fig. 5. Long-term offset drift of detectors. Shown for each wavelength are the mean, the maximum, and the standard deviation of the drift of all detector channels during one hour.

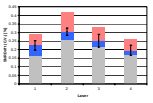

Fig. 6. Long-term drift of the noise in the optical signal. Shown for each wavelength are the mean, the minimum, and the maximum, and the standard deviation of signal C.V. for all channels during three hours of instrument operation.

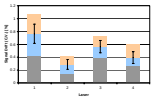

Fig. 7. Long-term stability of the optical signal. Shown for each wavelength are the mean, the minimum, and the maximum C.V. of the signal drift for all channels during three hours of instrument operation. The error bars depict the average drift C.V. of all channels.

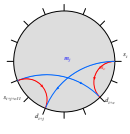

Fig. 8. Schematic illustration of the phantom-based calibration protocol as described in text. The optical signal transmitted by the phantom is assumed to depend only on the separation of S and D. According to the schematic and equation below, a quadruplet of readings can be used to cancel out the influence of source strengths and detector sensitivities, thus yielding estimates of η_i. These estimates are used to establish relative s_i and d_j values.

$$\frac{r_{i,j}}{r_{i,j+1}}\frac{r_{i+1,j+1}}{r_{i+1,j}} = \frac{s_i m_i d_{j+1} s_{i+1} m_{i+1} d_{j+1}}{s_i m_i d_{j+1} s_{i+1} m_{i+1} d_{j+1}} = \frac{m_i}{m_i} = 1$$

INSTRUMENT PERFORMANCE

1) Detector electronics noise/stability

Dark noise test of detector electronics:

- Detection of:
  - Component failure/aging in PMOD,
  - Problems with DAQ electronics
  - Deterioration of grounding connections, shielding
  - External sources of EM interferences
- Dark current is measured for each channel dependent on gain settings.
- Display of noise level (STD) and noise power spectrum.

2) Illumination noise/stability

- Illumination noise and drift is caused by:
  - Laser instabilities:
    - Typically long term (~sec - min)
    - Minimized by TEC control of laser operating temperature
    - Corrected by monitoring laser output power
  - Variation of the incoupling efficiency of the OS
    - Long term: thermal effects (heating of OS motor)
    - Short term: Frame-to-frame variations in illumination strength due to repeatability limits of the mechanical beam-steering mechanism.

Figs. 5-7 illustrate the measured noise and drift performance of the instrument.

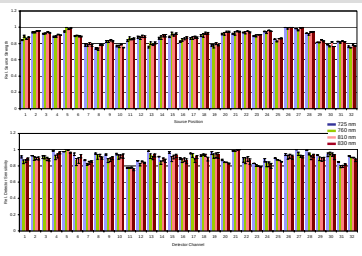

Fig. 9. Calibration results for 4-wavelength imager. A: s_i coefficients for four calibration measurements performed over the course of two days. All calibrations were performed on a Delrin cup (OD 63 mm, ID 57 mm) filled with diluted Intralipid (IL). The IL concentration was 0.5% for measurements 1-3 and 1.0% for the last measurement. Error bars indicate minimum and maximum values of the four experiments. B: d_j results for same study.

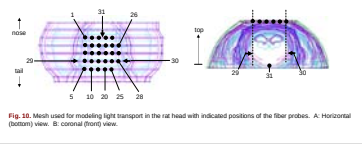

Fig. 10. Mesh used for modeling light transport in the rat head with indicated positions of the fiber probes. A: Horizontal (bottom) view. B: coronal (front) view.

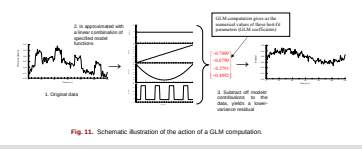

Fig. 11. Schematic illustration of the action of a GLM computation.

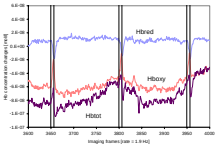

Fig. 12. Time series of the spatially averaged imaging results for the Hb states. Shown are three consecutive epochs of left front paw stimulation (no averaging over multiple epochs). Indicated are start and end of stimulation epochs. An early increase in Hboxy can be seen, followed by a delayed decrease in Hbred. The rise in Hboxy ends at the cessation of the stimlus, while Hbred shows delayed peaking. A biphasic Hbtot response is observed.

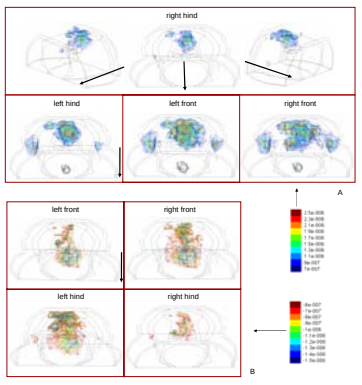

Fig. 13. GLM results for the reconstructed image time series for Hboxy (A) and Hbred (B). Shown are spatial maps of the GLM coefficients for the boxcar function representing periods of brain activation as estimated from the spatial average of the detector readings. The top row in panel A shows three different views to illustrate the spatial position of the activated area, all other results are shown only in a front/top view of the head. Arrows point toward the nose.

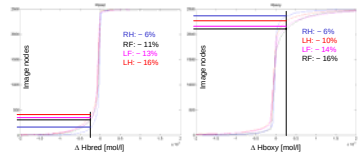

Fig. 14. Cumulative sum of the number of image nodes versus change in Hb state. Results are shown for the four stimulation sites (R=right, L=left, H= hind paw, F = fore paw) for Hbred (left) and Hboxy (right). The graphs indicate clear differences in the hemodynamic response to different stimulation sites. For example, a Hbred change of -0.25 µmol/l or stronger is seen in ~ 5% of the pixels for RH stimulation and in ~16% of the pixels for LH stimulation. Likewise, a Hboxy increase of 0.25 µmol/l or more is found in 6% of the image values for RH stimulation and in 16% of the pixels for the RF measurement.

3) Calibration protocol

A phantom measurement based calibration procedure has been introduced before, which allows determination of the relative inter-channel variation of the imager [3]:

- For a symmetric phantom, the light intensity transmitted from a source to a detector depends only on S - D separation (see Fig. 8)
- Deviations in the measured readings for different S/D pairs having the same probe separation can be attributed to instrumentation influences. These are numerically separated into differences in source strengths (expressed in source strength factors, $0 \le si \le 1$) and differences in detector sensitivity (expressed in detector sensitivity factors, $0 \le di \le 1$).

For equidistant placement of the probes along the perimeter of a cylindrical phantom (see Fig. 8), the measured signals can be modeled by matrix equation **R=SMD**. (**R**: matrix of the measured readings, **M**: matrix containing the fraction of intensity transmitted from Si to Dj through the medium, **S**, **D**: Matrices of source strength coefficients and detector sensitivity factors, respectively.)

- For a symmetric medium, **M** is always a constant-diagonal (TOEPLITZ) matrix.
- For a circular geometry, the symmetry of **M** can be used to obtain estimates of the entries m'_i of a matrix $\mathbf{M'} = a\,\mathbf{M}$.
- By creating the ratio $r_{ij}/m'_{ij} = a\,s_i d_j$ and dividing each resulting element by its row sum, a number proportional to d_j is obtained: $d'_j = m\,d_j$. Likewise, dividing elements $a\,s_i d_j$ by their column sum yields estimates of the source strength coefficients $s'_i = n\,s_i$.
- An electronic calibration was implemented to account for relative inter-channel variation of the detector gain settings.

Fig. 9 shows calibration results for the 4-WL imager.

FOUR-COLOR OPTICAL IMAGING OF THE RAT BRAIN

1) METHODS

i. Experimental protocol

- A male rat (approx. 400 g) was anesthetized, intubated, and positioned in the stereotaxic imaging head as seen in Fig. 2.
- 31 fiber optic probes were placed on the head as schematically indicated in Fig. 10:
  - 28 probes (channel numbers 1-28) were placed on the top of the head in a five-by-six rectangular grid with two corner positions left unoccupied.
  - Two probes (nos. 29, 30) were placed in the ears.
  - One probe was places inside the mouth.
- After instrument setup, a baseline measurement was performed for the duration of 1300 frames (~ 12 min)
- The baseline measurement was followed by electric stimulation of each of the four paws in the order right hind, left hind, left front, right front. Each paw was stimulated in six epochs which were applied every 150 imaging frames (79 s), with each epoch lasting six imaging frames (~ 3 s). Stimulation was performed with 5 mA ac current (10 Hz).

ii. Data analysis and image reconstruction

1. Data pre-processing:
   - Coefficients of variation (CV) were computed for all channels, and channels having CV values larger than 15% were excluded from further processing.
   - Raw data in the remaining channels were corrected for variations in laser power, which is monitored during the experiment.
   - For each channel, readings were normalized to the temporal mean value during the initial baseline period.
   - Data are subjected to an adaptive median filter to remove instantaneous negative spikes caused by measurement noise.
2. Image reconstruction
   - The weight matrix was computed using a finite element model (FEM) to numerically solve the diffusion equation. The FEM mesh (shown in Fig. 10) representing the anatomy of the rat head was adapted from [4]. For the current calculations, an optically homogeneous model was used.
   - Image reconstruction was achieved using the Normalized-Difference Method [5].
   - Truncated singular value decomposition (SVD) is used to solve the linear perturbation equation [6].
   - The reconstructed absorption coefficient images were used to compute image time series for oxygenated, deoxygenated, and total hemoglobin (Hboxy, Hbred, Hbtot, respectively) concentration changes.
3. Post-processing
   - A general linear model (GLM) algorithm [7] was used to find the best fit of each image node time series to a linear combination of four model functions, as schematically illustrated in Fig. 11.
     - The four model functions used were a constant (offset) term, linear and quadratic baseline drift functions, and a two-state boxcar function representing the idealized hemodynamic response of the brain to the stimulation.
     - The boxcar function was generated to reflect the periods of brain activation as determined from the raw spatial-averaged detector time series
     - The GLM coefficients for the boxcar function yield a representation of the spatially varying hemodynamic response to the stimulation.
   - No averaging over multiple epochs was performed for the analysis

2) RESULTS

i. Hemoglobin state time series

Fig. 12 shows the spatial average of the reconstructed image time series for the three Hb states during three consecutive stimulation epochs of the left front paw. Onset and cessation of each epoch are indicated.

- Hboxy concentration shows *increase* during stimulation:
  - Immediate rise (within one time frame ≅ 0.5 s) at the beginning of stimulus.
  - Steady increase during stimulation, peaking at the end of epoch.
  - Return to baseline starts immediately at end of epoch; return time ≅ rise time.
- Hbred concentration shows *decrease* during stimulation:
  - Similar (but inverted) shape and duration as the Hboxy curve.
  - Notable consistent time delay (~ one frame ≅ 0.5 s) between stimulation and response start.
  - Notable consistent time delay (~ one frame ≅ 0.5 s) between stimulation end and response peak.
- Hbtot concentration shows biphasic behavior:
  - Immediate rise (within one time frame ≅ 0.5 s) at epoch start.
  - Peaking after 4-5 frames (≅ 0.25 s).
  - Undershoot of baseline following stimulation.

ii. Reconstructed images

Fig. 13 shows spatial maps of the GLM coefficients for the boxcar model function computed on the reconstructed image time series for Hboxy and Hbred.

- The Hbred/Hboxy changes during stimulation occur primarily in a central region of the head that coincides with the location of the cortex. Some Hbred response can be seen in the outer regions of the head.
- Classic somatosensory activation is expected to be centralized for hind paw stimulation and lateralized for front paw stimulation. Right side stimulation is expected to activate the left portion of the cortex, and vice versa. Some spatial variation of the response to different stimulation sites – mostly in the extent of the response – is seen, but a clear somatosensory localization cannot be conclusively demonstrated.
- To gain a more quantitative understanding of the spatial extent of activation, we calculated the cumulative sum of image nodes showing a given change in Hb state (Fig. 14). The results show significant variation in the activated brain region for different stimulation sites.

CONCLUSION

- We presented data demonstrating the short and long term precision of the newly developed rat imager. Physiologic time series results show excellent measurement sensitivity to event related changes in Hb states in the rat brain.
- A phantom based calibration protocol and calibration results were presented.
- We demonstrated the capability of measuring individual activation epochs with high repeatability and signal quality allowing analysis of individual events without the requirement of averaging over multiple epochs.
- We proposed the following next steps to observe somatosensory localization of brain activity in the reconstruction results:
  - The stimulation parameters such as amplitude and duration need to be explored further.
  - We plan the refinement of the analysis. Possible strategies include the the use of more sophisticated model functions, the reconstruction of temporal features (such as delay times), the application of rate analysis, and the introduction of a more accurate optical model of the rat head.

REFERENCES

[1] C. H. Schmitz, M. Locker, J. M. Lasker, A. H. Hielscher, R. L. Barbour, "Instrumentation for fast functional optical tomography," *Review of Scientific Instruments*, Vol. 73, pp. 429-439 (2002).

[2] C. H. Schmitz, H. L. Graber, R. L. Barbour, J. M. Lasker, A. H. Hielscher, Y. Pei, "A real-time system for dynamic optical tomography," *OSA Biomedical Topical Meetings* (Miami Beach, FL, April 7-10, 2002), pp. 181-183.

[3] C. H. Schmitz, H. L. Graber, H. Luo, I. Arif, J. Hira, Y. Pei, A. Bluestone, S. Zhong, R. Andronova, J. Soller, N. Ramirez, S.-L. S. Barbour, R. L. Barbour, "Instrumentation and calibration protocol for imaging dynamic features in dense-scattering media by optical tomography," *Applied Optics*, Vol. 39, pp. 6466-6486 (2000).

[4] A. Y. Bluestone, M. Stewart, J. Lasker, G. S. Abdelaziz, A. H. H. Hielscher, "Three-dimensional Optical Tomographic Brain Imaging during Hypercapnia in Rodents," *Proc. SPIE* Vol. 4, pp. 115-123 (2003).

[5] Y. L. Pei, H. L. Graber, and R. L. Barbour, "Influence of systematic errors in reference states on image quality and on stability of derived information for DC optical imaging," *Applied Optics* Vol. 40, pp. 5755-5769 (2001).

[6] Y. Pei, H. L. Graber, and R. L. Barbour, "A fast reconstruction algorithm for implementation of time-series DC optical tomography," *Proc. SPIE* Vol. 4955, pp. 236-245 (2003).

[7] H. L. Graber, Y. Pei, R. L. Barbour, D. K. Johnston, Y. Zheng, and J. E. Mayhew, "Signal source separation and localization in the analysis of dynamic near-infrared optical tomographic time series," *Proc. of SPIE*, Vol.4955, pp. 31-51, (2003).

ACKNOWLEDGMENTS

This work was supported by the National Institutes of Health (NIH) under Grants 1R43CA91725-1A1, R21-HL67387, R21-DK63692 and R41-CA96102, by the Susan G. Komen Foundation under Grant IMG0403022, and by the US Army under Grant DAMD017-03-C-0018, and by the New York State Department of Health.